Journal of
Materials Chemistry A

ROYAL SOCIETY
OF CHEMISTRY

PAPER

View Article Online
View Journal | View Issue

Check for updates

Cite this: *J. Mater. Chem. A*, 2021, **9**, 20453

A comparative study of Bi, Sb, and BiSb for electrochemical nitrogen reduction leading to a new catalyst design strategy†

Youn Jeong Jang,‡[ab] Taylor A. Evans,‡[a] Bipasa Samanta,‡[c] Keyu Zeng,[a] Maytal Caspary Toroker *[cd] and Kyoung-Shin Choi *[a]

Recent studies identified Bi as one of the most promising non-noble metal elements that can promote the electrochemical N_2 reduction reaction (ENRR) to produce NH_3. The electronic features that make Bi a promising ENRR catalyst may also be owned by Sb that belongs to the same group as Bi. Thus, the ENRR properties of Bi, Sb, and a BiSb alloy were investigated comparatively to identify common characteristics that facilitate the ENRR. These catalysts were prepared as uniform coating layers on high surface area carbon felt electrodes, which could serve as both regular electrodes and pseudo-gas diffusion electrodes. The experimental results demonstrated that while Bi and Sb show comparable ENRR performances, the formation of a BiSb alloy distinctively increases the faradic efficiency for NH_3 production. The X-ray photoelectron spectroscopy results revealed that Bi in BiSb possesses a partial positive charge while Sb in BiSb possesses a partial negative charge, which can impact the way the catalyst surface interacts with the reactants and reaction intermediates of the ENRR and hydrogen evolution reaction (HER), the major competing reaction with the ENRR. Computational investigations including the Bader charge analysis and Gibbs free energy calculations for the elemental steps of the ENRR and HER provided an explanation of how the formation of a BiSb alloy can change the selectivity for the ENRR. The combined experimental and theoretical results and discussion contained in this study lead to a new strategy for designing efficient metal catalysts for the ENRR. Additionally, this study investigated how the use of gas phase and dissolved N_2 affected the ENRR performances of the Bi, Sb, and BiSb catalysts.

Received 23rd June 2021
Accepted 18th August 2021

DOI: 10.1039/d1ta05327b

rsc.li/materials-a

1. Introduction

Recently, the electrochemical nitrogen reduction reaction (ENRR) has greatly attracted research interest as a way to produce ammonia (NH_3) owing to the reduced cost of electricity generated using renewable energy. NH_3 is a key fertilizer, an important feedstock in industry, and a carbon-free energy source.[1–3] Unlike the traditional Haber-Bosch process, the ENRR produces NH_3 under ambient temperatures and pressures, using water as the hydrogen source.[4] Thus, it can offer an environmentally benign and sustainable route to produce NH_3. Furthermore, the ENRR can allow for the decentralized production of NH_3 in various capacities to suit the needs of those in remote areas, leading to reduced transportation and investment costs.[5]

The ENRR is currently impeded by the extremely low faradaic efficiency (FE) for the conversion of N_2 to NH_3. This low FE stems from two reasons. First, the standard reduction potential of N_2 to NH_3 ($N_2(g) + 8H^+ + 6e^- \rightleftharpoons 2NH_4^+(aq)$, $E^\circ = 0.275$ V *vs.* SHE) is very close to the standard reduction potential of the hydrogen evolution reaction (HER) ($2H^+ + 2e^- \rightleftharpoons H_2(g)$, $E^\circ = 0$ V *vs.* SHE).[8] Second, N_2 reduction to NH_3 is a much more kinetically complex process than the HER. As a result, the HER dominates under the applied potentials required for the ENRR. Thus, the discovery of new catalysts and strategies that can promote the ENRR is critically needed. The development of catalysts that do not contain noble metal elements are of particular interest as it can enable the production of ENRR catalysts on a practical scale.

Recent studies showed that Bi is one of the most promising non-noble metal elements that can promote the ENRR.[6–9] These observations may be related to a few features of Bi that can serve favorably for the ENRR. First, Bi has weak proton binding

---

[a] Department of Chemistry, University of Wisconsin–Madison, Madison, WI 53706, USA. E-mail: kschoi@chem.wisc.edu

[b] Department of Chemical Engineering, Hanyang University, Seongdong-gu, Seoul, 04763, Republic of Korea

[c] Department of Materials Science and Engineering, Technion—Israel Institute of Technology, Haifa 3200003, Israel. E-mail: maytalc@technion.ac.il

[d] The Nancy and Stephen Grand Technion Energy Program, Technion—Israel Institute of Technology, Haifa 3200003, Israel

† Electronic supplementary information (ESI) available. See DOI: 10.1039/d1ta05327b

‡ These authors contributed equally.

affinity and is poor at performing the HER.[10] Second, Bi is a semimetal and its conductivity is lower than typical metals.[11] It has been proposed that the rate of the HER is approximately first order with respect to the electron concentration, while the ENRR is zeroth order.[12] This means that as the availability of electrons decreases, the ENRR rate will not be strongly affected while the HER rate will decrease exponentially. Thus, the low conductivity of Bi may favorably act to increase the FE for NH_3 production. Third, it has also been demonstrated through density functional theory (DFT) calculations that the energy level of Bi 6p orbitals is advantageously positioned to interact with the N 2p orbitals, allowing for a stronger interaction between the Bi surface and a N_2 molecule and weakening the N_2 triple bond.[6]

The advantageous features of Bi for the ENRR motivated us to investigate the ENRR performance of Sb, another semi-metal directly above Bi in the periodic table, in comparison with that of Bi. Compared to Bi, Sb has received little attention as a possible ENRR catalyst, and there have been only a handful of studies of ENRR catalysts containing Sb.[13–15] The Sb-based catalysts used in these studies were composed of rather complex compositions and interfaces (*e.g.* antimony sulfide/tin oxide, antimony/antimony oxide, antimony phosphate/carbon). The ENRR property of pure Sb metal has not been investigated to date. Thus, comparing the ENRR performance of pure Sb metal in comparison with that of Bi can provide interesting new insights to understand the features of metals that can promote the ENRR.

The goal of the current study is two-fold. First, we aimed to prepare Bi, Sb, and a solid solution alloy BiSb with a 1 : 1 atomic ratio of Bi : Sb to comparatively study their ENRR performances. To obtain an accurate comparison, it is critical to prepare these catalysts with comparable morphologies and surface areas under similar synthesis conditions so that any difference observed in their ENRR performances is solely due to the difference in their compositions. Thus, we prepared Bi, Sb, and BiSb as uniform coating layers on a high surface area carbon felt substrate by electrodeposition and investigated their ENRR performances. Our experimental results show that the solid solution of BiSb shows a considerably enhanced ENRR performance compared with pure Bi and Sb. We conducted thorough computational investigations to elucidate the reason, which in turn provided a novel insight and general strategy that can be used to design efficient metal catalysts for the ENRR. The second goal is to examine if the performance of any of these catalysts can be improved if they can use N_2 gas directly instead of N_2 gas dissolved in the electrolyte for the ENRR. This allows us to study whether the low solubility of N_2 in the aqueous electrolyte (*ca.* 1 mM at 20 °C and 1 bar)[16] is one of the major limiting factors for the low FE for NH_3 production. For this purpose, we developed a simple method to use the same Bi, Sb, and BiSb electrodes on carbon felt both as a regular electrode and as a pseudo-gas diffusion electrode (GDE) so that the effect of using N_2 gas for the ENRR can be unambiguously identified.

We note that in this study, isotopically labeled $^{15}N_2$ was used as the N_2 source and only $^{15}NH_3$ was quantified to calculate the FE for NH_3 production. Thus, the effect of any environmental $^{14}NH_3$ contamination, which could result in the overestimation of the FE for NH_3 production, was completely eliminated.

2. Methods

2.1 Materials

Potassium antimony tartrate ($K_2Sb_2(C_4H_2O_6)_2 \cdot H_2O$, 99%), bismuth(III) nitrate ($Bi(NO_3)_3 \cdot 5H_2O$, ≥98.0%), sodium hydroxide (NaOH, ≥97.0%), ethylenediaminetetraacetic acid (EDTA, 99.4–100.6%), boric acid (H_3BO_3, ≥99.5%), potassium pyrophosphate ($K_4P_2O_7$, 97%), tartaric acid ($C_4H_6O_6$, ≥99.5%), hydrochloric acid (HCl, 37%), 4-(dimethylamino)benzaldehyde ($C_9H_{11}NO$, 99%), hydrazine hydrate ($N_2H_4 \cdot xH_2O$, 50–60%), phosphoric acid (H_3PO_4, 85%), deuterated water (D_2O, 99.9%) and ammonium chloride ($^{15}NH_4Cl$, 99%) were all purchased from Millipore-Sigma. All chemicals were used as received and without further purification. Carbon felt (AvCarb C100) was purchased from Fuel Cell Store for use as the working electrode. Deionized (DI) water with a resistivity of >18.0 MΩ cm was used to prepare all solutions.

2.2 Synthesis of Bi, Sb, and BiSb

Electrodeposition was carried out in an undivided three electrode cell composed of a carbon felt working electrode, a Ag/AgCl (4 M KCl) reference electrode and a carbon rod counter electrode using a VMP2 multichannel potentiostat (Princeton Applied Research). The working electrode was prepared by first cutting carbon felt into 5 cm × 1 cm × 0.3 cm strips. Then, the top portion of the carbon felt electrodes was tightly wrapped with Teflon tape (J.V. Converting Company) to prevent solution from traveling up the carbon felt and making direct contact with the conducting alligator clip, which connects the carbon felt to the lead from the potentiostat. The size of the carbon felt electrode exposed to the solution was 2 cm × 1 cm × 0.3 cm. All current densities reported in this study are the currents divided by the largest lateral area (2 cm × 1 cm) of the carbon felt substrate.

For Bi deposition, the aqueous plating solution contained 20 mM $Bi(NO_3)_3 \cdot 5H_2O$ and 1 M tartaric acid with the pH adjusted to 6 with NaOH. The films were deposited using a pulsed deposition where a short pulse of potential is applied followed by a resting time at the open circuit potential (OCP). Each cycle was composed of applying a potential of −0.9 V *vs.* AgCl for five seconds followed by a resting time of ten seconds, and the cycle was repeated for 24 times to pass approximately 1.6 C of charge. The pulsed deposition was critical for the deposition of Bi as a uniform layer. For Sb deposition, the aqueous plating solution contained 10 mM $K_2Sb_2(C_4H_2O_6)_2 \cdot H_2O$ and 1 M tartaric acid with the pH adjusted to 7.5 with NaOH. The films were deposited onto carbon felt by applying −1.4 V *vs.* Ag/AgCl for 20 seconds, passing approximately 1.6 C of charge. For the deposition of BiSb, an aqueous plating solution containing 20 mM $Bi(NO_3)_3 \cdot 5H_2O$, 30 mM $K_2Sb_2(C_4H_2O_6)_2 \cdot H_2O$, and 1 M tartaric acid with the pH adjusted to 6 with NaOH was used. The films were deposited by applying −1.5 V *vs.* Ag/AgCl for 20 seconds to pass approximately 1.6 C of charge. Before deposition of any species onto the carbon felt substrate, the carbon felt working electrode was immersed in a tartate solution (pH ∼7) that did not contain Bi or Sb, and the potential was swept from the OCP to −1.7 V *vs.* Ag/AgCl. This process ensured sufficient wetting of the surface of the carbon felt substrate before electrodeposition, allowing for more uniform coverage of the deposits on the substrate.

2.3 Characterization

Powder X-ray diffraction (PXRD, D8 Discover, Bruker, Ni-filtered Cu Kα radiation, $\lambda = 1.5418$ Å) was used to examine the crystal structure of the electrodes. Scanning electron microscopy with an accelerating voltage of 2 keV (SEM; LEO Supra55 VP) and energy dispersive spectroscopy with an accelerating voltage of 22 keV (EDS; Noran System Seven, Thermo-Fisher, ultra-dry silicon drift detector) were used to investigate the morphology and bulk elemental ratios respectively. X-ray photoelectron spectroscopy (XPS) using a Thermo Scientific K-Alpha X-ray photoelectron spectrometer equipped with an Al Kα excitation source was used to determine surface elemental compositions.

2.4 Electrochemical characterization

All electrochemical measurements were performed in an undivided three electrode cell. Either Sb, Bi or BiSb on carbon felt was used as the working electrode, with a Ag/AgCl (3 M KCl) reference electrode and a carbon rod counter electrode. The stainless-steel cell used in this study has a cover with a gas inlet and an outlet to allow for gas purging. Before any electrochemical measurement, the solution was saturated with Ar (99.999%) or $^{15}N_2$ and during the measurement the gas was purged constantly. When the catalyst electrode was used as a regular electrode, $^{15}N_2$ was purged through a needle inserted into the electrolyte. The purging needle was approximately 1 cm apart from the catalyst electrode, and the rate of gas flow was 100 mL min^{-1}. When the catalyst electrode was used as a pseudo-GDE, the purging needle was inserted into the middle of the carbon felt substrate as illustrated in Scheme 1. The needle had multiple holes on the side to purge N_2 to all directions within the substrate. The rate of gas flow was varied from 50 mL min^{-1} to 200 mL min^{-1} to find an optimal rate.

In this study, all ENRR experiments were performed with isotopically labeled $^{15}N_2$ as the N_2 source and only $^{15}NH_3$ (not $^{14}NH_3$) was quantified to calculate the FE for NH_3 production.[17] This was to eliminate any concern from a possible environmental $^{14}NH_3$ contaminant falsely affecting the FE for NH_3 production. The purity of the isotopically labelled $^{15}N_2$ gas is 98% ^{15}N and ≥99.0% N_2 ($^{15}N_2$ + $^{14}N_2$) with the remaining <1% impurities identified by the manufacturer (Sigma-Aldrich) as Ar, O_2, CO_2, N_2O, and C_2H_6. To remove any nitrogen-containing impurities in the N_2 gas flow, the $^{15}N_2$ gas was first passed through a Cu/SAPO trap as recommended in the literature.[17]

The linear sweep voltammograms (LSVs) were obtained in 0.5 M borate (pH 9.3) by sweeping the potential from the OCP to the negative direction with the scan rate of 25 mV s^{-1}. Constant potential ENRR was performed in the same solution by applying a desired potential and passing 10 C. All constant potential ENRRs were repeated with Ar instead of $^{15}N_2$ to confirm the produced $^{15}NH_3$ came from the reduction of $^{15}N_2$ gas. Before any measurements, a potential of −0.6 V *vs.* RHE for 1 minute was applied to reduce the naturally formed oxide passivation layer on the metal surfaces.

Proton nuclear magnetic resonance (^{1}H-NMR) was used to quantify the produced $^{15}NH_3$ on a Bruker Advance III HD 600 MHz spectrometer (Bruker Biospin Corp., Billerica, MA) equipped with a TCI-F cryoprobe with *z*-gradient. After the *J*–*t* measurement, the electrolyte was collected and acidified to pH ∼3 using H_3PO_4 and then condensed to 6 mL using reduced pressure distillation. After this, 5 v% D_2O with trimethylsilylpropanoic acid (TSP) was mixed with the solution to act as the internal reference for locking. The ^{1}H signal from the water was removed using water suppression with excitation sculpting. The quantification of $^{15}NH_3$ was not affected by water suppression because the $^{15}NH_4{}^+$ signal appears at 7 ppm. Spectra were acquired using 1024 scans, a relaxation delay of 1.5 s and an acquisition time of 3 s. A calibration curve was prepared using solutions of a known concentration of $^{15}NH_4Cl$ in the same electrolyte used for the *J*–*t* measurements followed by the above

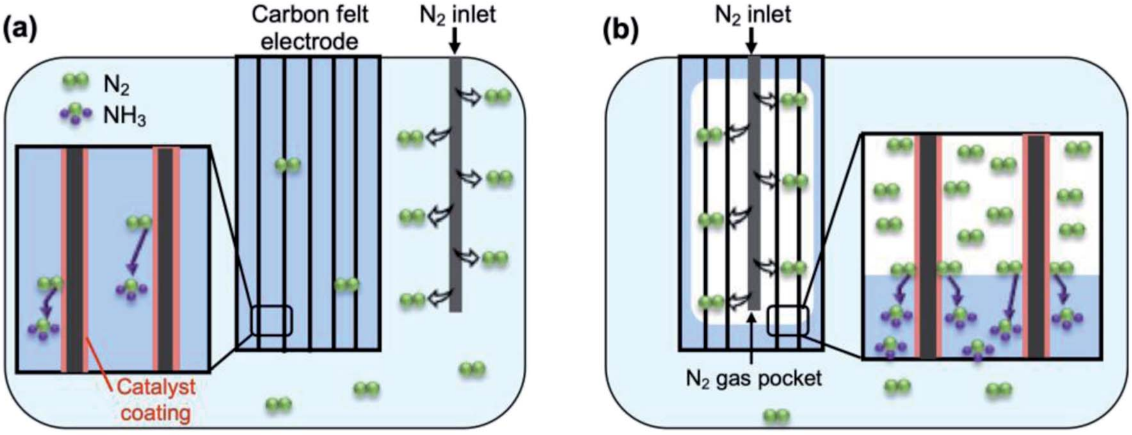

Scheme 1 An illustration of how our Bi, Sb, and BiSb electrodes can be used as (a) a regular electrode and (b) a pseudo-GDE.

acidification and mixing with D_2O containing TSP for locking and integrating the observed $^{15}NH_4^+$ signal for each.

The ENRR can also produce N_2H_4, therefore the Watt and Crisp method was used to determine if any N_2H_4 formed during the ENRR.[18] After the ENRR, 2 mL of the electrolyte was collected in a centrifuge tube and 2 mL of ethanol solution containing 0.7 M HCl and 0.12 M 4-(dimethylamino)benzaldehyde was added. The solution was left to react for 1 hour at room temperature and then the absorbance was measured at 455 nm using a UV-VIS spectrophotometer. The concentration of N_2H_4 was determined by comparing the measured absorbance to a calibration curve generated using standard solutions of N_2H_4 prepared by adding $N_2H_4 \cdot xH_2O$ into the electrolyte used in *J–t* measurements. No N_2H_4 was detected for any of the *J–t* measurements. The FE for NH_3 was determined using the following equation where *F* is Faraday's constant (96485.33 C mol^{-1}):

$$\text{FE }(\%) = \frac{3 \times n_{\text{NH}_3}(\text{mol}) \times F(\text{C mol}^{-1})}{\text{total charged passed (C)}} \times 100 \tag{1}$$

While a Ag/AgCl reference was used in each experiment performed, all results within this report are presented against the reversible hydrogen electrode (RHE) for direct comparison to other reports in aqueous solution but that contain different pH values. The conversion between Ag/AgCl and RHE reference electrode values can be done *via* the following equation:

$$E_{(vs.\ \text{RHE})} = E_{(vs.\ \text{Ag/AgCl})} + E_{(\text{Ag/AgCl})}(\text{reference}) + 0.0591\ \text{V} \times \text{pH (at 25 °C)} \tag{2}$$

$$E_{\text{Ag/AgCl}}(\text{reference, 4 M KCl}) = 0.1976\ \text{V}\ vs.\ \text{NHE at 25 °C}$$

$$E_{\text{Ag/AgCl}}(\text{reference, 3 M KCl}) = 0.209\ \text{V}\ vs.\ \text{NHE at 25 °C}$$

2.5 Computational methods

In order to understand the key factors that make BiSb a better ENRR catalyst than Bi and Sb, Density Functional Theory (DFT) calculations were performed using the Vienna *ab Initio* Simulation Package (VASP).[19–21] Spin-polarized DFT[22,23] calculations were performed using the generalized gradient approximation of Perdew, Burke, and Ernzerhof (PBE).[24] The utility of the PBE functional for modeling the nitrogen reduction reaction (NRR) on the current system has been already well established.[25–28] The frozen core electrons of Bi 1s2s2p3s3p3d4s4p4d5s5p4f, Sb 1s2s2p3s3p3d4s4p4d and N 1s are presented by the projected augmented wave (PAW) method.[20]

For the initial bulk system, we have taken a rhombohedral structure with a *R*3*m* space group for all three systems (Bi, Sb and BiSb).[29,30] After the initial convergence test for energy cut off and *K*-point, we have obtained an energy cut off value of 450 eV for the Bi and BiSb systems and 300 eV for the Sb system for a converged energy of 1 meV per atom (Fig. S1†). The converged *K*-point for the bulk systems is 16 × 16 × 6 gamma points. From the optimized bulk (Table S1†) we have obtained the (012) surface of Bi, Sb, and BiSb to study for the ENRR (Fig. S2†). The (012) plane was chosen because it is the most densely packed plane and is mentioned to be more catalytic for the ENRR than other low indexing planes.[26,28,31] Due to these reasons, the (012) plane has been most intensively investigated for the ENRR on Bi.[28,31,32] For the slab optimization we have taken 5 × 5 × 1 gamma *K*-points with the vacuum of 15 Å in the *z* direction. The energy and force convergence criteria of 1×10^{-5} eV and -0.02 eV Å^{-1} are employed respectively in all the calculations.

The Gibbs free energy (ΔG) of each elemental step is calculated using the following equation (Tables S2 and S3†).[33]

$$\Delta G = \Delta E + \Delta E_{\text{ZPE}} - T\Delta S \tag{3}$$

where ΔE, ΔE_{ZPE} and ΔS denote the change of total energy, zero-point energy, and entropy at 298.15 K, respectively. The computational hydrogen electrode (CHE)[33,34] was employed in this ENRR study. In the CHE method the chemical potential of the proton–electron pair is equal to one-half of the chemical potential of gaseous H_2. This potential value of the proton–electron pair is used to calculate the Gibbs free energy of the intermediates involved in the ENRR, as the intermediates are formed by H^+ addition to a N_2 molecule. Apart from ΔG, we have also calculated Bader charges[35] of the surfaces to describe the catalytic properties. The configurations of N_2 and other intermediate species on the catalyst surfaces determined by these calculations are shown in Fig. S3–S6.†

3. Results and discussion

3.1 Synthesis of Bi, Sb, and BiSb electrodes

Bi, Sb and BiSb were deposited on the carbon felt substrate to investigate their ENRR performances. The carbon felt substrate not only provided a high surface area to deposit Bi, Sb and BiSb but also allowed the resulting Bi, Sb and BiSb electrodes to be tested both as regular electrodes and as pseudo-GDEs, as explained in detail below.

In order to accurately compare the ENRR performances of Bi, Sb and BiSb, they must be prepared with comparable morphologies and surface areas so that the difference in their ENRR performances solely originates from the difference in their compositions, and is not affected by any difference in their morphologies. Thus, we aimed to deposit Bi, Sb and BiSb as featureless conformal coating layers on the carbon felt substrate using plating solutions whose compositions are comparable with each other. We discovered that tartrate solutions (pH 6–7.5) can solubilize both Bi^{3+} and Sb^{3+} ions and allow Bi, Sb, and BiSb to be deposited as uniform coating layers on the carbon felt substrate (Fig. 1). The same amount of charge was passed to deposit each of these layers to ensure that the thicknesses of all catalyst layers are comparable (150–200 nm) (Fig. S7†).

The XRD patterns of Bi, Sb, and BiSb deposited on carbon felt are shown in Fig. 2. In the XRD patterns, broad peaks originating from the carbon felt were commonly observed. The Bi and Sb electrodes show Bi peaks and Sb peaks, respectively, indicating that the as-deposited Bi and Sb layers are crystalline, although the

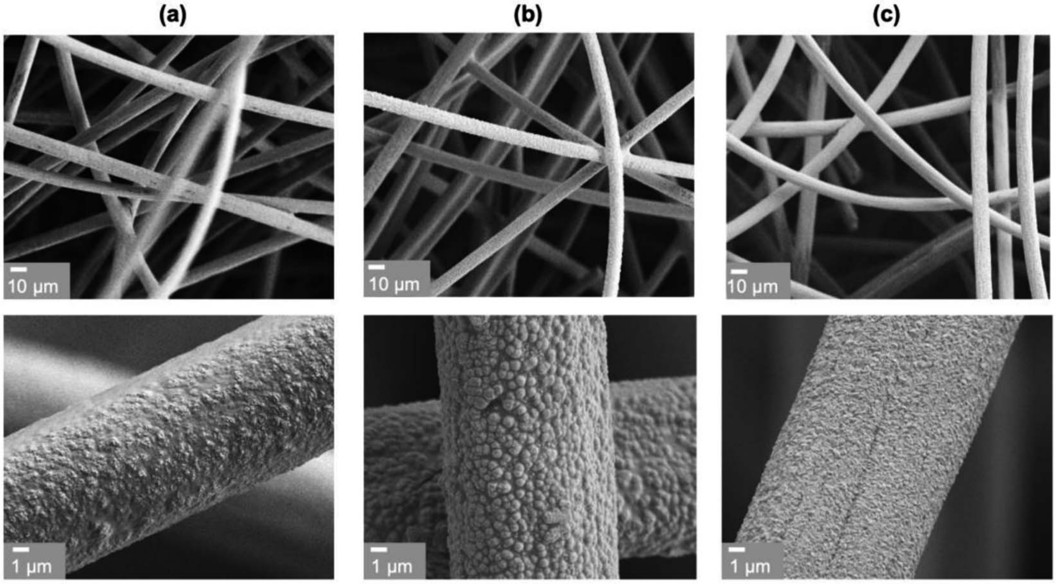

Fig. 1 SEM images of (a) Bi, (b) Sb, and (c) BiSb deposited on the carbon felt substrate. The bottom panels show corresponding higher-magnification images of Bi, Sb, and BiSb deposits on a single carbon fiber.

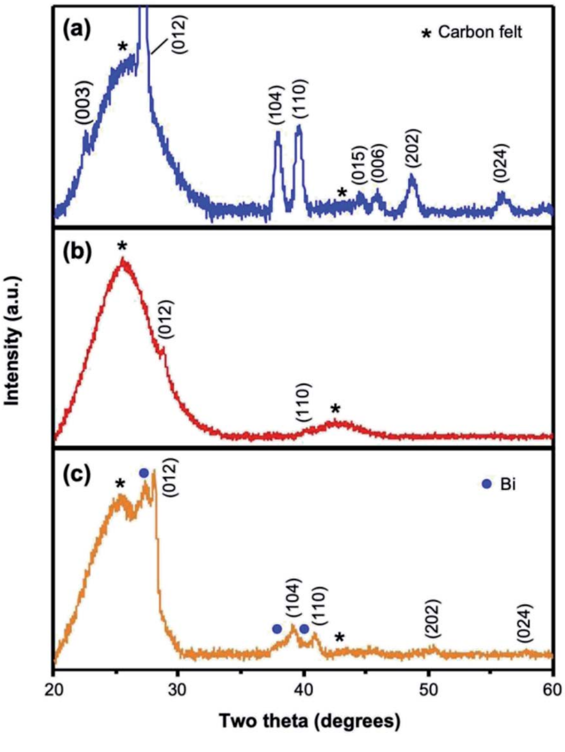

Fig. 2 XRD patterns of as-deposited (a) Bi, (b) Sb, and (c) BiSb on carbon felt. The (*hkl*) indices are assigned from the PDF cards for Bi (44-1246) and Sb (35-0732). The broad peaks corresponding to the carbon felt are denoted by an asterisk. Bi ($R\bar{3}m$, $a = 0.454650$ nm and $c = 1.186294$ nm), Sb ($R\bar{3}m$, $a = 0.430777$ nm and $c = 1.127662$ nm) and BiSb ($R\bar{3}m$, $a = 0.442680$ nm and $c = 1.160351$ nm).[36]

crystallinity of the Sb layer appears to be significantly lower than that of the Bi layer. We note that Bi and Sb have the same crystal structure, and the only difference is that Sb has smaller cell parameters,[36] which shift the Sb peaks to higher two theta values. BiSb also has the same crystal structure, and its (*hkl*) peaks appear exactly at the positions expected for a solid solution alloy of Bi and Sb with the Bi : Sb ratio of 1 : 1, whose unit cell parameters are the averages of the unit cell parameters of Bi and Sb.[36]

The XRD of the BiSb electrode also shows peaks from Bi, meaning Bi is present as an impurity phase in the BiSb electrode. The EDS analysis, which analyzes the bulk composition of the sample, showed that the Bi : Sb ratio in the BiSb electrode is 2 : 1. However, the XPS analysis, which analyzes the surface composition of the sample, showed that the Bi : Sb ratio in the BiSb electrode is 1 : 1, which agrees with the Bi : Sb ratio in the BiSb alloy. Combining the results from XRD, EDS, and XPS, the BiSb sample appeared to contain a pure Bi layer as the bottom layer and a 1 : 1 BiSb alloy layer as the top layer with the amount of Bi in the Bi layer and that in the BiSb layer to be approximately 1 : 1. The formation of a Bi layer as the bottom layer could not be avoided because the onset potential for the reduction of Bi^{3+} to Bi^0 is significantly more positive than that of Sb^{3+} to Sb^0 in the tartrate solutions used in this study (Fig. S8†). This means that when the deposition of BiSb was accomplished using a deposition potential that is negative enough to reduce both Bi^{3+} and Sb^{3+}, the overpotential applied for Bi deposition is significantly larger than that for Sb deposition. Thus, Bi was deposited first before Bi and Sb are co-deposited with the 1 : 1 ratio. Since XPS confirmed that the top layer is a pure 1 : 1 BiSb alloy, the fact that the BiSb electrode contains Bi as the bottom layer did not affect our goal of comparing the ENRR performances of Bi, Sb, and BiSb.

3.2 ENRR performance of Bi, Sb, and BiSb as regular electrodes and pseudo-GDEs

As we mentioned earlier, one of the major goals of the current study is to examine whether the low solubility of N_2 gas in aqueous electrolytes (*e.g.* 1.4 mM N_2 at 20 °C)[16] is one of the main reasons for low FEs for NH_3 production and whether the use of a GDE, which can directly utilize the gas phase N_2 as the reactant, can enhance the FE for NH_3 production. Our Bi, Sb, and BiSb electrodes deposited on the carbon felt substrate allow us to use the same electrodes as a regular electrode and as a pseudo-GDE as explained in Scheme 1.

Scheme 1a shows the case where these electrodes are used as regular electrodes. In this set-up, $^{15}N_2$ is provided by a $^{15}N_2$-purging needle immersed in the electrolyte. The solution is pre-saturated with $^{15}N_2$ and $^{15}N_2$ is also constantly purged during the reaction with a gas flow rate of 100 mL min^{-1}. The catalyst coating on the carbon felt form the catalyst/electrolyte interface and the catalysts will utilize dissolved $^{15}N_2$ for the ENRR. Scheme 1b shows the case where these electrodes are used as a pseudo-GDE. In this case, the $^{15}N_2$-purging needle is placed in the middle of the carbon felt electrode. The $^{15}N_2$ gas comes out from the multiple side openings of the needle, expelling the solution to create a gas pocket within the carbon felt electrode. By adjusting the rate of $^{15}N_2$ gas coming out from the openings of the needle (50–200 mL min^{-1}), an optimal three-phase interface among the $^{15}N_2$ gas pocket, solid catalyst on the carbon fibers, and liquid electrolyte that contains water as the hydrogen source can be created.

The pseudo-GDE used in this study is the same as a true GDE in that it allows the catalyst to directly utilize gas phase N_2 for the ENRR by creating the three-phase interface.[37] However, unlike the preparation of a true GDE,[37] no alteration for the substrate structure, catalyst preparation, and cell configuration was necessary for the conversion of a regular electrode to a pseudo-GDE in our study. Thus, its use in comparison with the use of the same electrode as a regular electrode allowed us to directly assess the change in the ENRR performances caused only by the use of gas phase N_2 *versus* dissolved N_2.

The ENRR performance of the Bi electrode as a regular electrode was first investigated by comparing LSVs obtained in 0.5 M borate (pH 9.3) saturated with either Ar or $^{15}N_2$ (Fig. 3a, top). When the electrolyte was saturated with Ar, the hydrogen evolution reaction (HER) was the only reduction reaction that could occur. The reason why the LSV showed cathodic current even before the potential reaches the thermodynamic onset potential for the HER (0 V *vs.* RHE) is due to the high surface area carbon felt electrode creating high charging current when sweeping the potential. Since the charging current profile is not

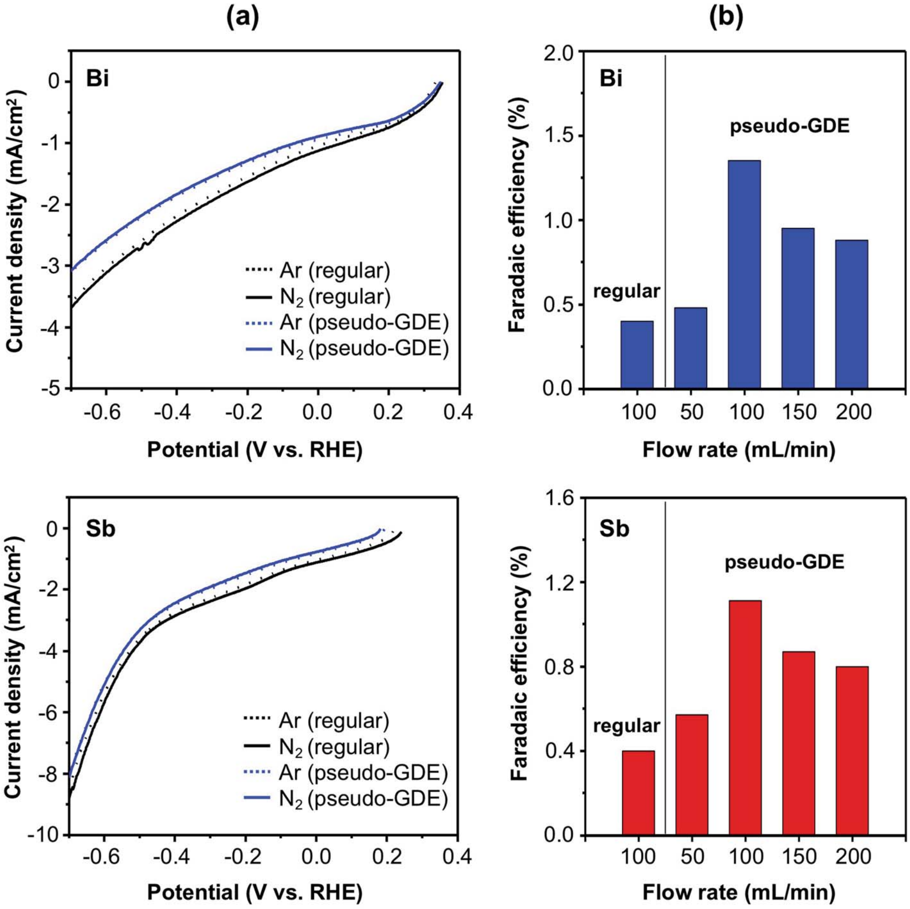

Fig. 3 (a) LSVs of Bi (top) and Sb (bottom) as a regular electrode (black) and as a pseudo-GDE (blue) in 0.5 M borate (pH 9.3) with Ar (dotted) or $^{15}N_2$ (solid) (scan rate, 25 mV s^{-1}). The gas flow rate was 100 mL min^{-1} for all cases. (b) FEs for $^{15}NH_3$ of Bi (top) and Sb (bottom) as a regular electrode and as a pseudo-GDE with various $^{15}N_2$ flow rates at −0.6 V *vs.* RHE.

completely flat, it is rather difficult to know the exact onset potential for the HER. When the electrolyte is saturated with $^{15}N_2$, little change in current density was observed in the LSV. This does not necessarily mean that Bi cannot conduct the ENRR because if Bi performs the ENRR using a fraction of electrons that would otherwise be used for the HER, the total current density would not change. Thus, in order to examine whether or not the ENRR occurs on the Bi electrode, a constant potential reduction and product analysis was necessary.

When the ENRR was performed at a constant potential of −0.6 V *vs.* RHE, a FE of 0.4% for NH_3 production was observed (Fig. 3b, top). The Bi electrode shows a negligible ENRR activity at potentials more positive than −0.6 *vs.* RHE (Table S4†).

Next, the ENRR performance of the Bi electrode as a pseudo-GDE was investigated using the setup shown in Scheme 1b. The LSVs obtained with a gas flowing rate of 100 mL min^{-1} is shown in Fig. 3a, top. The LSV of Bi as a pseudo-GDE obtained with Ar shows a slight decrease in the current density compared with that of Bi as a regular electrode. This is because purging Ar within the carbon felt electrode created a gas pocket inside the carbon felt electrode, decreasing the electrode surface area that is in contact with the electrolyte. This decreases the electrode area that can perform the HER.

When $^{15}N_2$ was purged instead of Ar in the pseudo-GDE, a similar decrease in the current density was observed in the LSV due to the same reason. Since the major reaction that occurs on the electrode is the HER, the decrease in the electrode/electrolyte area resulted in the decrease in the total current density even if the FE for the ENRR may increase. The LSVs obtained with various flow rates of $^{15}N_2$ (50–200 mL min^{-1}) can be found in Fig. S9,† where a gradual decrease in the total current density is shown with an increase in the N_2 flow rate.

We performed the ENRR at a constant potential of −0.6 V *vs.* RHE using Bi as a pseudo-GDE with various flow rates of N_2 and quantified the produced NH_3 (Fig. 3b, top). The highest FE for NH_3 production (1.3%) was obtained with the $^{15}N_2$ flow rate of 100 mL min^{-1}, and this FE is approximately three times higher than that obtained with Bi as a regular electrode. When the flow rate is lower than 100 mL min^{-1}, it appeared that not a sufficient $^{15}N_2$ pocket was developed to convert the Bi electrode to an effective pseudo-GDE. On the other hand, when the flow rate is higher than the optimal rate, the supply of $^{15}N_2$ is no longer a limiting factor for the ENRR. It appears that an unnecessarily high flow rate can disrupt the formation of an optimal three-phase interfacial structure in our pseudo-GDE system.

Our result demonstrated that the use of a pseudo-GDE can certainly enhance the FE for NH_3 production. However, the FE for NH_3 is still low, suggesting that the low solubility of N_2 is not the most critical limiting factor for the low FE for NH_3 production when a Bi metal layer with an intrinsically limiting ENRR catalytic property is used as the electrode.

The Sb electrodes were investigated using the same procedures (Fig. 3, bottom and Fig. S9b†). Again, the LSVs obtained with Ar and $^{15}N_2$ look comparable and the LSV obtained using Sb as a pseudo-GDE shows a slight decrease in the current density compared with that obtained with Sb as a regular electrode (Fig. 3a, bottom). When the ENRR was performed at a constant potential of −0.6 V *vs.* RHE, the FE for $^{15}NH_3$ production was 0.4% as a regular electrode and 1.1% as a pseudo-GDE with the N_2 flow rate of 100 mL min^{-1} (Fig. 3b, bottom), showing that the use of a GDE can enhance the ENRR performance of Sb by approximately three times. When the Sb electrode was used as a pseudo-GDE with various $^{15}N_2$ flow rate, the FE obtained with the flow rate of 100 mL min^{-1} was the highest as in the case of Bi. The catalytic behaviors of Sb are comparable to those of Bi. However, Sb appears to be slightly inferior to Bi in terms of FE for NH_3 production.

There may be a concern that the carbon felt used as the substrate may contain nitrogen species, which can be reduced to NH_3 during the ENRR, and falsely increase the FE for NH_3. We examined that the N_{1s} region of the XPS spectrum of the carbon felt and confirmed the absence of nitrogen on the carbon felt surface (Fig. S10†). More importantly, we note that our FEs for NH_3 were calculated based only on the amount of $^{15}NH_3$ detected, and $^{14}NH_3$ was not counted as the N_2 reduction

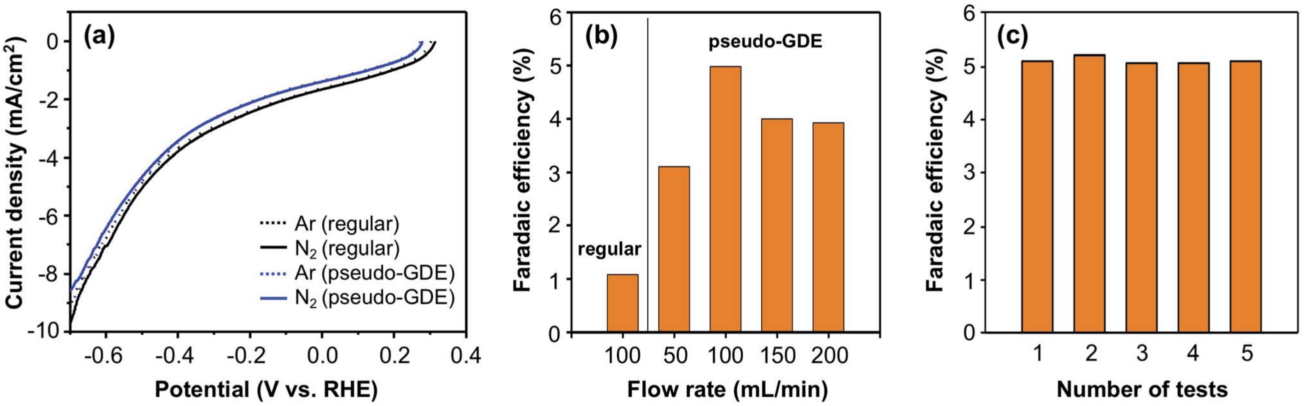

Fig. 4 (a) LSVs of BiSb as a regular electrode (black) and as a pseudo-GDE (blue) in 0.5 M borate (pH 9.3) with Ar (dotted) or $^{15}N_2$ (solid) (scan rate, 25 mV s^{-1}). The gas flow rate was 100 mL min^{-1} (b) FEs for $^{15}NH_3$ of BiSb as a regular electrode and as a pseudo-GDE with various $^{15}N_2$ flow rates at −0.6 V *vs.* RHE. (c) FEs for $^{15}NH_3$ of BiSb as a pseudo-GDE with the N_2 flow rate of 100 mL min^{-1} at −0.6 V *vs.* RHE for five consecutive experiments.

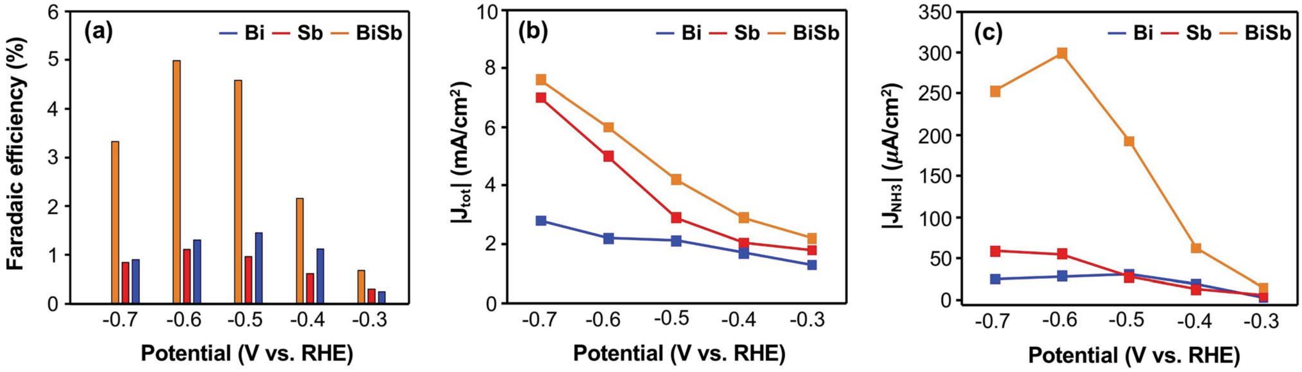

Fig. 5 (a) FEs for NH_3, (b) total current densities, and (c) partial current densities associated with $^{15}NH_3$ production by Bi, Sb, and BiSb pseudo-GDE electrodes with the N_2 flow rate of 100 mL min^{-1} in 0.5 M borate (pH 9.3).

product. Thus, even if the nitrogen species in the carbon felt were reduced to $^{14}NH_3$, it would not affect our FE results. We also performed the ENRR with $^{15}N_2$ using a bare carbon felt electrode at −0.6 V *vs.* RHE and detected no $^{15}NH_3$. This confirms that all $^{15}NH_3$ detected in our experiments was truly from the reduction of $^{15}N_2$ by Bi or Sb.

The ENRR performance of BiSb was examined using the same procedures (Fig. 4a and S9c†). Fig. 4a shows the LSVs of the BiSb electrode as a regular electrode and as a pseudo-GDE obtained in 0.5 borate (pH 9.3). As in the case of Bi and Sb, no noticeable difference in the LSVs was observed when the solution was purged with Ar or $^{15}N_2$. Also, as in the case of Bi and Sb, the current density obtained using the BiSb electrode as a pseudo-GDE was slightly lower than the current density obtained using BiSb as a regular electrode.

When a constant potential ENRR was performed at −0.6 V *vs.* RHE, the BiSb electrode showed a considerably higher FE for $^{15}NH_3$ production (Fig. 4b) than those obtained with the Bi and Sb electrodes. When used as a regular electrode, the FE for $^{15}NH_3$ production by BiSb was 1.1%, which is more than a two-fold increase from those by Bi and Sb electrodes. When used as a pseudo-GDE, the FE for NH_3 reaches 5.0% at a $^{15}N_2$ flow rate of 100 mL min^{-1}, which is more than a four-fold increase from those of Bi or Sb alone (as in the case of Bi and Sb, the highest FE was obtained when the N_2 flow rate was 100 mL min^{-1}). We also note that the enhancement in FE observed by the use of a pseudo-GDE is the greatest for BiSb; the supply of $^{15}N_2$ can be a more limiting factor for a better ENRR catalyst. We conducted the constant potential ENRR four more times using the same BiSb pseudo-GDE (Fig. 4c) and obtained the same level of FE for NH_3, which confirms the stability of the BiSb electrode.

In Fig. 5a, the FEs for NH_3 production by Bi, Sb, and BiSb as pseudo-GDEs are compared at various potentials when the $^{15}N_2$ flow rate is fixed as 100 mL min^{-1}. The FEs for NH_3 production by BiSb are significantly higher than those by Bi and Sb at all potentials and is at a maximum at −0.6 V *vs.* RHE. We also compared the total current densities of the three pseudo-GDEs obtained at various constant potentials. We note that the current density is as important as the FE as the rate of NH_3 production is governed by both factors. If the increase in FE is accompanied by a decrease in current density, no net gain may be obtained in terms of the production rate and yield of NH_3. Our results show that the total current densities generated by the BiSb electrode during the constant potential ENRR at all potentials are also higher than those by Bi and Sb (Fig. 5b). Owing to the combination of enhanced FEs for NH_3 production and enhanced current densities, the partial current densities for NH_3 production by BiSb, which directly affect the production rate of NH_3, are much higher than those of Bi and Sb (Fig. 5c). The production rates of NH_3 by Bi, Sb and BiSb used as a pseudo-GDE are summarized in Table 1. The original *J–t* plots of Bi, Sb and BiSb obtained from the constant potential ENRR at various potentials are shown in Fig. S11.†

It is worth mentioning that while the FE values for NH_3 production reported in this study may seem low compared with FE values reported in a few recent studies,[6–9] the partial current density achieved by BiSb for NH_3 production is considerable (Fig. 5c) because the total current density generated by BiSb is high (*e.g.*, ∼6 mA cm^{-2} at −0.6 V *vs.* RHE) (Fig. 5b). The robustness of the BiSb alloy catalyst, which makes it possible to electrodeposit the catalyst with no delicate nanoscale morphology control or defect control, can be a practical advantage of BiSb.

Our result that BiSb exhibits a considerably better ENRR performance for the ENRR is intriguing considering that BiSb is a solid solution of Bi and Sb, which at first does not seem to possess any unique features not owned by Bi or Sb. In order to investigate the reason for the enhanced ENRR of BiSb, we

Table 1 Production rates of $^{15}NH_3$ by Bi, Sb, and BiSb pseudo-GDE electrodes with the $^{15}N_2$ flow rate of 100 mL min^{-1} in 0.5 M borate (pH 9.3)

Potential V *vs.* RHE	Production rate (μg cm^{-2} h^{-1})		
	Bi	Sb	BiSb
−0.3	0.73	1.21	3.31
−0.4	4.26	2.80	14.00
−0.5	6.88	6.23	43.05
−0.6	6.40	12.42	66.90
−0.7	5.64	13.16	56.66

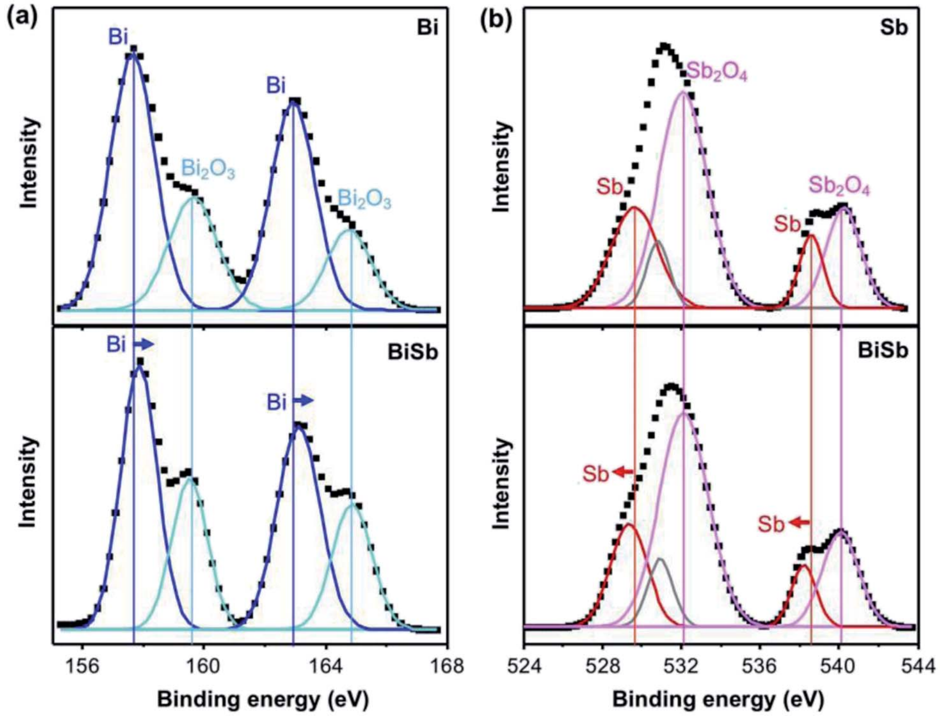

Fig. 6 XPS spectra of the (a) Bi 4f region of Bi (top) and BiSb (bottom) and (b) Sb 3d region of Sb (top) and BiSb (bottom) (black squares: experimental data, blue line: Bi metal peak, light blue line: Bi_2O_3 peak, red line: Sb metal peak, pink line: Sb_2O_4 peak, gray line: oxygen 1s peak).

examined the XPS spectra of Bi, Sb, BiSb, which revealed surprising results. Fig. 6a shows the Bi 4f peaks of Bi and BiSb. Since Bi is not a noble metal, its surface is oxidized to Bi_2O_3. Thus, the Bi 4f region of the Bi electrode shows Bi peaks from Bi metal and also from a surface Bi_2O_3 layer.[38,39] We note that the ENRR results we obtained were not affected by the presence of the Bi_2O_3 layer because the surface oxide layer was electrochemically pre-reduced to Bi prior to the ENRR (see the Methods section). The Bi_2O_3 detected by XPS was formed after the ENRR experiment when Bi was exposed to the air before the XPS measurements, which was unavoidable. The Bi 4f region of BiSb also shows Bi peaks from Bi metal and Bi_2O_3. However, the positions of the Bi peaks of BiSb are shifted to a higher binding energy compared with the positions of the Bi peaks of Bi, suggesting that Bi in BiSb bears a partial positive charge. The Bi_2O_3 peaks of BiSb do not show the same shift compared with the Bi_2O_3 peaks of Bi, meaning that the shifts of the Bi peaks of BiSb are not due to any systematic error but truly due to an intrinsic difference in the charge of Bi in Bi and BiSb.

Fig. 6b shows the Sb 3d peaks of Sb and BiSb. Since Sb is not a noble metal, its surface is also oxidized. Thus, the Sb 3d region of the Sb electrode shows peaks from Sb metal and a surface Sb_2O_4 layer.[39–42] Again, since we pre-reduced the catalyst surface before the ENRR, our ENRR results were not affected by the surface oxide layer, and the Sb_2O_4 layer formed in the air after the ENRR is irrelevant to the ENRR performance. The Sb 3d region of the BiSb electrode also shows peaks from Sb and Sb_2O_4. This time, while the positions of the Sb_2O_4 remain the same, the Sb peaks of BiSb are clearly shifted to lower binding energy, meaning that Sb in BiSb possess a partial negative charge.

The XPS results indicate that Bi in BiSb bears a slightly positive charge and Sb in BiSb bears a slightly negative charge. The polarity between Bi and Sb in BiSb is unexpected as the electronegativities of Bi and Sb are very similar (2.02 for Bi and 2.05 for Sb).[43] Nonetheless, the partial positive charge on Bi and the partial negative charge on Sb created by the formation of a BiSb alloy is most likely the key to explain the enhanced ENRR performances of BiSb compared with Bi and Sb metals that bear no charges. Thus, we turned to computational studies to confirm the charge distribution in BiSb and compare the surface properties and thermodynamics of Bi, Sb, and BiSb relevant to the ENRR.

3.3 Computational results

The charge of atoms on the catalyst surface can affect the binding strength and charge transfer between the catalyst surface and reactant species. Thus, we first performed Bader charge analysis on the (012) planes of Bi, Sb, and BiSb to examine whether the alloy formation can affect the charge distribution on Bi and Sb atoms. The reason for selecting the (012) plane is described in the method section, and the analysis results are summarized in Fig. 7. Fig. 7(i) shows that all atoms on the Bi and Sb surfaces contain slightly negative charges. However, when Bi and Sb form a 1 : 1 alloy, Bi atoms develop distinctive positive charges while Sb atoms develop distinctive negative charges. These results agree well with the experimental results obtained from the XPS analysis.

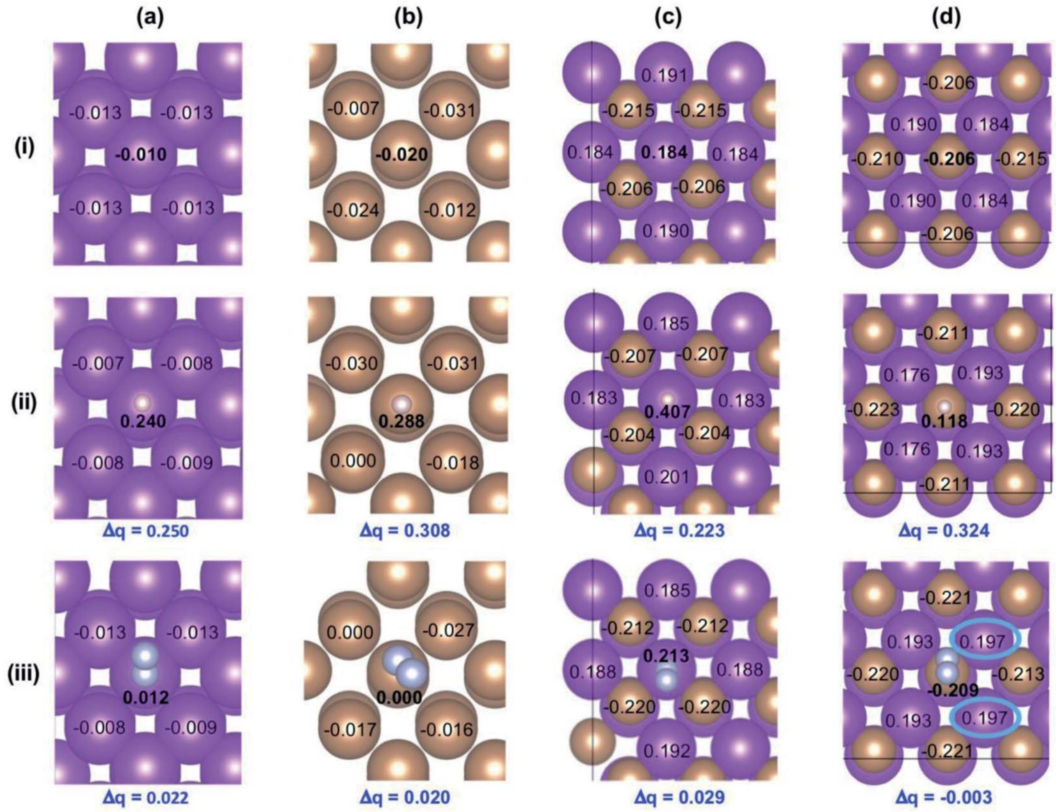

Fig. 7 Bader charge analysis of (a) Bi, (b) Sb, (c) Bi in BiSb, and (d) Sb in BiSb on their (012) planes; (i) the pristine surface, (ii) the surface when H is adsorbed and (iii) the surface when N_2 is adsorbed (Bi: violet, Sb: golden, N: gray, and H: beige). The atomic charges are indicated on the corresponding atoms. Δq represents the change in charge at the binding site after H or N_2 adsorption. In (d(iii)), the blue circles represent charges on Bi atoms that changed considerably by N_2 adsorption on Sb.

Next, we examined how the charges on the Bi, Sb and BiSb surfaces affect the adsorption of H, which is the critical step for the HER, the major competing reaction with the ENRR. Fig. 7(ii) shows the charges on Bi, Sb, Bi in BiSb, and Sb in BiSb after the adsorption of H. A greater change in charge at the binding site before and after H adsorption means a greater amount of charge transferred from the metal site to H and a stronger adsorption of H. The results show that adsorption strength of H is in the order of Sb in BiSb > Sb > Bi > Bi in BiSb. When we examined the changes of the charges on the catalyst surfaces after N_2 adsorption, an opposite trend was observed. Fig. 7(iii) shows that change in the charge before and after N_2 adsorption, which is equivalent to the adsorption strength of N_2, is in the order of Bi in BiSb > Bi > Sb > Sb in BiSb.

The greatest amount of charge transferred from Bi in BiSb to N_2 can be explained by considering the interaction of both the lone pair orbital and π^* orbital of N_2 with the metal atoms. Unlike H, N_2 has lone pair electrons that can be donated to the metal binding site to form a sigma bond. Thus, Bi in BiSb that bears positive charges and can act as a Lewis acid, forms a stronger sigma bond with N_2 compared with Bi, Sb, or Sb in BiSb that possess negative charges. The stronger sigma bond between Bi in BiSb and N_2 in turn allows for a stronger π back bonding between them so that a greater amount of charge can be transferred from Bi in BiSb to the π^* orbital of N_2, which will more effectively activate the triple bond in N_2. The Sb in BiSb shows negligible change in the charge before and after N_2 adsorption. However, it is worth noting that the Bi atoms next to Sb show a noticeable increase in positive charge after N_2 adsorption on Sb (blue circles in Fig. 7d(iii)), meaning that charge transfer occurs from neighboring Bi atoms to N_2 adsorbed on Sb *via* the orbital interaction between Bi and Sb. In this case, the adsorption strength of N_2 on Sb in BiSb may be stronger than that predicted by considering the change in charge only on the Sb binding site. In fact, ΔG for N_2 adsorption discussed below suggests that N_2 adsorption on Sb in BiSb is as favorable as that on Bi in BiSb. After N_2 adsorption on Sb, the positive charges accumulated on the neighboring Bi atoms may further promote the adsorption of N_2 on these Bi atoms.

The results obtained from the Bader charge analysis indicates that between Bi and Sb in BiSb, Bi is the more active site for the ENRR; the positive charges on Bi developed by the formation of a BiSb alloy makes the Bi sites more favorable for N_2 adsorption but less favorable for H adsorption than Bi or Sb alone. Thus, it appears that the Bi site in BiSb is responsible for BiSb achieving a higher FE for NH_3 production than Bi or Sb alone.

To further analyze the catalytic difference caused by the formation of a BiSb alloy, we calculated the Gibbs free energy of

Table 2 ΔG values for N_2 adsorption, $\Delta G_{\mathrm{PDS}}^{\mathrm{ENRR}}$, and $\Delta G_{\mathrm{PDS}}^{\mathrm{HER}}$ (in eV) for various metal sites. The PDS for the ENRR is the formation of adsorbed NNH, and the PDS for the HER is the formation of adsorbed H

Site	ΔG for N_2 adsorption	$\Delta G_{\mathrm{PDS}}^{\mathrm{ENRR}}$	$\Delta G_{\mathrm{PDS}}^{\mathrm{HER}}$
Bi	0.098	1.912	0.627
Bi in BiSb	0.020	2.020	0.680
Sb in BiSb	0.021	1.968	0.460
Sb	0.111	1.964	0.521

each elemental step involved with the ENRR. According to a literature survey there are two mechanisms: dissociative and associative (Fig. S12†).[44,45] In the dissociative pathway, the triple bond in N_2 is broken first, and the resulting two N atoms adsorb on two different catalytic sites (Fig. S12a†). Since N_2 adsorbs very weakly on Bi, Sb, and BiSb, it is highly improbable that the triple bond in N_2 is cleaved during the initial adsorption step. Hence, the energetically unfavorable dissociative pathway was not considered in our calculations. In the associative mechanism there are also two pathways, the alternate pathway and the distal pathway (Fig. S12b and c†).[26,44–46] The Gibbs free energy for the elemental steps of alternate and distal pathways are provided in Tables S5 and S6.† The configurations of N_2 and other intermediate species on the catalyst surfaces are shown in Fig. S3–S6.† Our results show that the alternate pathway is thermodynamically more favored than the distal pathway for all catalysts investigated in this study and that the formation of the intermediate species NNH, which is the common step for both pathways, is the potential determining step (PDS) for the ENRR for all catalysts (Tables S5 and S6†). Table 2 summarizes the ΔG for N_2 adsorption, ΔG for the PDS of the ENRR ($\Delta G_{\mathrm{PDS}}^{\mathrm{ENRR}}$), and ΔG for the PDS of the HER ($\Delta G_{\mathrm{PDS}}^{\mathrm{HER}}$), which is the adsorption of H, for all catalysts. The rest of the ENRR steps are thermodynamically more favorable than the N_2 adsorption and the formation of NNH.

The results in Table 2 revealed that the formation of BiSb does not result in a decrease in $\Delta G_{\mathrm{PDS}}^{\mathrm{ENRR}}$. Instead, the formation of BiSb makes the N_2 adsorption on BiSb more favorable than that on Bi or Sb. This makes N_2 adsorption more facile and increases the N_2 coverage on BiSb, enhancing the FE for the ENRR. The comparison of $\Delta G_{\mathrm{PDS}}^{\mathrm{HER}}$ values revealed another effect of forming BiSb; the HER becomes less favorable on Bi in BiSb than on Bi alone while the HER becomes more favorable on Sb in BiSb than on Sb alone, which agrees well with the results obtained from the Bader charge analysis. Combining all results, it can be concluded that the formation of BiSb facilitates N_2 adsorption on the Bi site and also makes the HER less favorable on the Bi site, thus enhancing the ENRR on the Bi site in BiSb. This also means that Bi in BiSb is the active site for ENRR and is what makes BiSb a better ENRR catalyst than Bi or Sb. On the other hand, by forming BiSb, the Sb site becomes more effective for the HER. However, since HER is the dominant reaction anyway on Bi or Sb alone, the formation of a BiSb alloy, which makes 50% of its surface (*i.e.*, Bi sites) more catalytic for the ENRR can increase the FE for the ENRR.

4. Conclusions

In summary, we prepared Bi, Sb, and a BiSb alloy as uniform coating layers on a high surface area carbon felt electrode so that any difference observed in their ENRR performances could solely be due to the difference in their compositions. The resulting electrodes served as both regular electrodes and pseudo-GDEs for us to investigate the difference in using dissolved N_2 and gas phase N_2 as the reactant. Our experimental results showed that the formation of a BiSb alloy can considerably enhance the ENRR performance in terms of both FE and the rate for NH_3 production compared with pure Bi or Sb. Also, the enhancement in the FE for NH_3 production caused by using the electrode as a pseudo-GDE was greatest for BiSb. Computational investigations revealed that the formation of a BiSb alloy resulted in the development of a partial positive charge on Bi in BiSb and a partial negative charge on Sb in BiSb, which was experimentally confirmed by XPS results. The Bader charge analysis showed that the partial charges developed in BiSb allowed for stronger N_2 adsorption on the BiSb surface than the surface of Bi or Sb. Also, from the Gibbs free energy calculations for the elemental steps involved with the ENRR and HER, it was demonstrated that Bi in BiSb makes the PDS of the HER (*i.e.* the adsorption of H) more difficult than pure Bi or Sb, thus enhancing the ENRR. In other words, Bi in BiSb is the more active site for the ENRR and makes BiSb a better ENRR catalyst than Bi or Sb.

Our combined experimental and computational study suggests that producing an alloy where one metal type develops a partial positive and the other develops a partial negative charge can be an effective general strategy to increase the strength of N_2 adsorption on a metal catalyst surface. We have recently demonstrated that maintaining positively charged Bi^{3+} on a Bi metal catalyst during the ENRR by the formation of surface layers (*e.g.* $BiPO_4$, $Bi(PO_4)_{1-x}(VO_4)_x$) that are more difficult to reduce than Bi_2O_3 is an effective strategy to enhance the FE for the ENRR.[9] However, Bi^{3+} in any compound must be eventually reduced to Bi^0 when a more reductive bias is applied to increase the rate of NH_3 production. However, BiSb is an alloy composed of Bi and Sb metal atoms that cannot be further reduced. Thus, the partial positive charge developed on Bi in BiSb cannot be further reduced under the reductive bias conditions and can promote N_2 adsorption even in the high overpotential region. In the same manner, other metal ENRR catalysts can perform better when forming alloys if the formation of alloys results in the development of partial charges that can enhance N_2 adsorption or formation of ENRR intermediates.

Conflicts of interest

The authors declare no competing interests.

Acknowledgements

The experimental study of the work was supported by the Division of Chemical Sciences, Geosciences, and Biosciences, Office of Basic Energy Sciences of the U.S. Department of Energy through Grant DE-SC0008707. The computational study of the work was supported by the Nancy and Stephen Grand Technion Energy Program, the Ministry of Science and Technology (MOST) of Israel, and the COST Action 18234 supported by COST (European Cooperation in Science and Technology). Y. J. Jang acknowledges financial support by the National Research Foundation of Korea (NRF) grant funded by the Korea (MSIT) (No. 2021R1A4A3027878, No. 2021R1F1A1063146) and the research fund of Hanyang University (HY-202000000000520). The authors thank Prof. Daniel C. Fredrickson for his help with initial Bader charge analysis.

References

1 A. Klerke, C. H. Christensen, J. K. Nørskov and T. Vegge, Ammonia for hydrogen storage: challenges and opportunities, *J. Mater. Chem.*, 2008, **18**, 2304–2310.

2 J. W. Erisman, M. A. Sutton, J. Galloway, Z. Klimont and W. Winiwarter, How a century of ammonia synthesis changed the world, *Nat. Geosci.*, 2008, **1**, 636–639.

3 V. Smil, Detonator of the population explosion, *Nature*, 1999, **400**, 415.

4 J. G. Chen, R. M. Crooks, L. C. Seefeldt, K. L. Bren, R. M. Bullock, M. Y. Darensbourg, P. L. Holland, B. Hoffman, M. J. Janik, A. K. Jones, M. G. Kanatzidis, P. King, K. M. Lancaster, S. V. Lymar, P. Pfromm, W. F. Schneider and R. R. Schrock, Beyond fossil fuel–driven nitrogen transformations, *Science*, 2018, **360**, eaar6611.

5 B. H. R. Suryanto, H.-L. Du, D. Wang, A. N. Simonov and D. R. MacFarlane, Challenges and prospects in the catalysis of electroreduction of nitrogen to ammonia, *Nat. Catalysis.*, 2019, **2**, 290–296.

6 Y. C. Hao, Y. Guo, L. W. Chen, M. Shu, X. Y. Wang, T. A. Bu, W. Y. Gao, N. Zhang, X. Su, X. Feng, J. W. Zhou, B. Wang, C. W. Hu, A. X. Yin, R. Si, Y. W. Zhang and C. H. Yan, Promoting nitrogen electroreduction to ammonia with bismuth nanocrystals and potassium cations in water, *Nat. Catal.*, 2019, **2**, 448–456.

7 Y. Wang, M.-M. Shi, D. Bao, F.-l. Meng, Q. Zhang, Y.-T. Zhou, K.-H. Liu, Y. Zhang, J.-z. Wang, Z.-w. Chen, D.-p. Liu, Z. Jiang, M. Luo, L. Gu, Q.-h. Zhang, X.-z. Cao, Y. Yao, M.-H. Shao, Y. Zhang, X.-B. Zhang, J. G. Chen, J.-M. Yan and Q. Jiang, Generating Defect-Rich Bismuth for Enhancing the Rate of Nitrogen Electroreduction to Ammonia, *Angew. Chem. Int. Edit.*, 2019, **58**, 9464–9469.

8 L. Li, C. Tang, B. Xia, H. Jin, Y. Zheng and S.-Z. Qiao, Two-Dimensional Mosaic Bismuth Nanosheets for Highly Selective Ambient Electrocatalytic Nitrogen Reduction, *ACS Catal.*, 2019, **9**, 2902–2908.

9 Y. J. Jang and K.-S. Choi, Enabling electrochemical N_2 reduction to NH_3 in the low overpotential region using non-noble metal Bi electrodes via surface composition modification, *J. Mater. Chem. A.*, 2020, **8**, 13842–13851.

10 S. Trasatti, Work function, electronegativity, and electrochemical behaviour of metals: III. Electrolytic hydrogen evolution in acid solutions, *J. Electroanal. Chem.*, 1972, **39**, 163–184.

11 J. P. Issi, Low Temperature Transport Properties of Group V Semimetals, *Aust. J. Phys.*, 1979, **32**, 585–628.

12 A. R. Singh, B. A. Rohr, J. A. Schwalbe, M. Cargnello, K. Chan, T. F. Jaramillo, I. Chorkendorff and J. K. Nørskov, Electrochemical Ammonia Synthesis—The Selectivity Challenge, *ACS Catal.*, 2017, **7**, 706–709.

13 L. Di, X. Chen, Y.-T. Liu, J. Yu and B. Ding, Sb_2S_3 nanoparticles anchored on SnO_2 nanofibers: a high-performance hybrid electrocatalyst toward ammonia synthesis under ambient conditions, *Chem. Commun.*, 2019, **55**, 13892–13895.

14 M. Bat-Erdene, G. Xu, M. Batmunkh, A. S. R. Bati, J. J. White, M. J. Nine, D. Losic, Y. Chen, Y. Wang, T. Ma and J. G. Shapter, Surface oxidized two-dimensional antimonene nanosheets for electrochemical ammonia synthesis under ambient conditions, *J. Mater. Chem. A*, 2020, **8**, 4735–4739.

15 X. Liu, H. Jang, P. Li, J. Wang, Q. Qin, M. G. Kim, G. Li and J. Cho, Antimony-Based Composites Loaded on Phosphorus-Doped Carbon for Boosting Faradaic Efficiency of the Electrochemical Nitrogen Reduction Reaction, *Angew. Chem. Int. Edit.*, 2019, **58**, 13329–13334.

16 N. I. Kolev, Solubility of O_2, N_2, H_2, and CO_2 in water. in, *Multiphase Flow Dynamics*, Springer, Berlin, 1st edn, 2011.

17 S. Z. Andersen, V. Čolić, S. Yang, J. A. Schwalbe, A. C. Nielander, J. M. McEnaney, K. Enemark-Rasmussen, J. G. Baker, A. R. Singh, B. A. Rohr, M. J. Statt, S. J. Blair, S. Mezzavilla, J. Kibsgaard, P. C. K. Vesborg, M. Cargnello, S. F. Bent, T. F. Jaramillo, I. E. L. Stephens, J. K. Nørskov and I. Chorkendorff, A rigorous electrochemical ammonia synthesis protocol with quantitative isotope measurements, *Nature*, 2019, **570**, 504–508.

18 G. W. Watt and J. D. Chrisp, Spectrophotometric Method for Determination of Hydrazine, *Anal. Chem.*, 1952, **24**, 2006–2008.

19 G. Kresse and J. Furthmüller, Efficient iterative schemes for ab initio total energy calculations using a plane-wave basis set, *Phys. Rev. B: Condens. Matter Mater. Phys.*, 1996, **54**, 11169–11186.

20 G. Kresse and D. Joubert, From Ultrasoft Pseudopotentials to the Projector Augmented-Wave Method, *Phys. Rev. B: Condens. Matter Mater. Phys.*, 1999, **59**, 1758–1775.

21 G. Kresse and J. Furthmüller, Efficiency of Ab-Initio Total Energy Calculations for Metals and Semiconductors Using a Plane-Wave Basis Set, *Comput. Mater. Sci.*, 1996, **6**, 15–50.

22 P. Hohenberg and W. Kohn, Inhomogeneous Electron Gas, *Phys. Rev.*, 1964, **136**, B864–B871.

23 W. S. L. J. Kohn, Self-Consistent Equations Including Exchange and Correlation Effects, *Phys. Rev.*, 1965, **140**, A1133–A1138.

24 J. P. Perdew, K. Burke and M. Ernzerhof, Generalized Gradient Approximation Made Simple, *Phys. Rev. Lett.*, 1996, **77**, 3865.

25 Y. Lin, L. Yang, H. Jiang, Y. Zhang, Y. Bo, P. Liu, S. Chen, B. Xiang, G. Li, J. Jiang, Y. Xiong and L. Song, Sulfur

Atomically Doped Bismuth Nanobelt Driven by Electrochemical Self-Reconstruction for Boosted Electrocatalysis, *J. Phys. Chem. Lett.*, 2020, **11**, 1746–1752.

26 Y.-C. Hao, Y. Guo, L.-W. Chen, M. Shu, X.-Y. Wang, T.-A. Bu, W.-Y. Gao, N. Zhang, X. Su, X. Feng, J.-W. Zhou, B. Wang, C.-W. Hu, A.-X. Yin, R. Si, Y.-W. Zhang and C.-H. Yan, Promoting Nitrogen Electroreduction to Ammonia with Bismuth Nanocrystals and Potassium Cations in Water, *Nat. Catal.*, 2019, **2**, 448–456.

27 Y. Wang, M. M. Shi, D. Bao, F. L. Meng, Q. Zhang, Y. T. Zhou, K. H. Liu, Y. Zhang, J. Z. Wang, Z. W. Chen, D.-P. Liu, Z. Jiang, M. Luo, L. Gu, Q.-H. Zhang, X.-Z. Cao, Y. Yao, M.-H. Shao, Y. Zhang, X.-B. Zhang, J. G. Chen, J.-M. Yan and Q. Jiang, Generating Defect-Rich Bismuth for Enhancing the Rate of Nitrogen Electroreduction to Ammonia, *Angew. Chem., Int. Ed.*, 2019, **58**, 9464–9469.

28 Y. Yang, J. Li, K. Chen, Q. J. Chen and Y. Feng, Catalytic Performance of Two-Dimensional Bismuth Tuned by Defect Engineering for Nitrogen Reduction Reaction, *J. Phys. Chem. C*, 2020, **124**(36), 19563–19570.

29 Y. Nie, M. Rahman, D. Wang, C. Wang and G. Guo, Strain induced topological phase transitions in monolayer honeycomb structures of group-V binary compounds, *Sci. Rep.*, 2015, **5**, 1–6.

30 C. S. Barrett, The structure of bismuth at low temperatures, *Aust. J. Phys.*, 1960, **13**, 209–222.

31 L. Li, C. Tang, B. Xia, H. Jin, Y. Zheng and S.-Z. Qiao, Two-Dimensional Mosaic Bismuth Nanosheets for Highly Selective Ambient Electrocatalytic Nitrogen Reduction, *ACS Catal.*, 2019, **9**, 2902–2908.

32 R. Zhang, L. Ji, W. Kong, H. Wang, R. Zhao, H. Chen, T. Li, B. Li, Y. Luo and X. Sun, Electrocatalytic N_2-to-NH_3 conversion with high faradaic efficiency enabled using a Bi nanosheet array, *Chem. Commun.*, 2019, **55**(36), 5263–5266.

33 E. Skulason, T. Bligaard, S. Gudmundsdottir, F. Studt, J. Rossmeisl, F. Abild-Pedersen, T. Vegge, H. Jonsson and J. K. Norskov, A Theoretical Evaluation of Possible Transition Metal Electro-Catalysts for N_2 Reduction, *Phys. Chem. Chem. Phys.*, 2012, **14**, 1235–1245.

34 J. H. Montoya, C. Tsai, A. Vojvodic and J. K. Norskov, The Challenge of Electrochemical Ammonia Synthesis: A New Perspective on the Role of Nitrogen Scaling Relations, *ChemSusChem*, 2015, **8**, 2180–2186.

35 G. Henkelman, A. Arnaldsson and H. Jónsson, A fast and robust algorithm for Bader decomposition of charge density, *Comput. Mater. Sci.*, 2006, **36**, 354–360.

36 J. Berger, B. Christ and J. Troschke, Lattice Parameter Study in the $Bi_{1\text{-}x}Sb_x$ Solid-solution System, *Cryst. Res. Technol.*, 1982, **17**, 1233–1239.

37 D. Higgins, C. Hahn, C. Xiang, T. F. Jaramillo and A. Z. Weber, Gas-Diffusion Electrodes for Carbon Dioxide Reduction: A New Paradigm, *ACS Energy Lett.*, 2019, **4**, 317–324.

38 V. S. Dharmadhikari, S. R. Sainkar, S. Badrinarayan and A. Goswami, *J. Electron Spectrosc. Relat. Phenom.*, 1982, **25**, 181–189.

39 L. Escobar-Alarcón, J. Morales-Mendez, D. Solís-Casados, S. Romero, M. Fernández and E. Haro-Poniatowski, *J. Phys.: Conf. Ser.*, 2015, **582**, 012013.

40 F. Garbassi, XPS and AES study of antimony oxides, *Surf. Interface Anal.*, 1980, **2**, 165–169.

41 R. Izquierdo, E. Sacher and A. Yelon, X-ray photoelectron spectra of antimony oxides, *Appl. Surf. Sci.*, 1989, **40**, 175–177.

42 T. A. Evans and K.-S. Choi, Electrochemical Synthesis and Investigation of Stoichiometric, Phase-Pure $CoSb_2O_6$ and $MnSb_2O_6$ Electrodes for the Oxygen Evolution Reaction in Acidic Media, *ACS Appl. Energy Mater.*, 2020, **3**, 5563–5571.

43 L. Pauling, *The Nature of the Chemical Bond*, Cornell University Press, Ithaca, New York, 3rd edn, 1960.

44 R. Zhao, H. Xie, L. Chang, X. Zhang, X. Zhu, X. Tong, T. Wang, Y. Luo, P. Wei, Z. Wang and X. Sun, Recent Progress in the Electrochemical Ammonia Synthesis under Ambient Conditions, *EnergyChem*, 2019, **1**, 100011.

45 X. Cui, C. Tang and Q. Zhang, A Review of Electrocatalytic Reduction of Dinitrogen to Ammonia under Ambient Conditions, *Adv. Energy Mater.*, 2018, **8**, 1800369.

46 H.-R. Zhu, Y.-L. Hu, S.-H. Wei and D.-Y. Hua, Single-Metal Atom Anchored on Boron Monolayer (β12) as an Electrocatalyst for Nitrogen Reduction into Ammonia at Ambient Conditions: A First-Principles Study, *J. Phys. Chem. C*, 2019, **123**, 4274–4281.